RESEARCH ARTICLE

Magnetic Resonance in Medicine

Ultra-short T_2 components imaging of the whole brain using 3D dual-echo UTE MRI with rosette k-space pattern

Xin Shen[1] | Ali Caglar Özen[2] | Antonia Sunjar[1] | Serhat Ilbey[2] |
Stephen Sawiak[3,4] | Riyi Shi[1,5] | Mark Chiew[6] | Uzay Emir[1,7]

[1]Weldon School of Biomedical Engineering, Purdue University, West Lafayette, Indiana USA

[2]Department of Radiology, Medical Physics, Medical Center–University of Freiburg, Faculty of Medicine, University of Freiburg, Freiburg, Germany

[3]Department of Clinical Neurosciences, University of Cambridge, Cambridge, UK

[4]Department of Psychology, University of Cambridge, Cambridge, UK

[5]College of Veterinary Medicine, Purdue University, West Lafayette, Indiana USA

[6]Wellcome Centre for Integrative Neuroimaging, University of Oxford, Oxford, UK

[7]School of Health Sciences, Purdue University, West Lafayette, Indiana USA

Correspondence
Uzay Emir, Purdue University, School of Health Sciences, 550 Stadium Mall Drive, West Lafayette, IN, USA.
Email: uemir@purdue.edu

Purpose: This study aimed to develop a new 3D dual-echo rosette k-space trajectory, specifically designed for UTE MRI applications. The imaging of the ultra-short transverse relaxation time (uT_2) of brain was acquired to test the performance of the proposed UTE sequence.

Theory and Methods: The rosette trajectory was developed based on rotations of a "petal-like" pattern in the k_x–k_y plane, with oscillated extensions in the k_z-direction for 3D coverage. Five healthy volunteers underwent 10 dual-echo 3D rosette UTE scans with various TEs. Dual-exponential complex model fitting was performed on the magnitude data to separate uT_2 signals, with the output of uT_2 fraction, uT_2 value, and long-T_2 value.

Results: The 3D rosette dual-echo UTE sequence showed better performance than a 3D radial UTE acquisition. More significant signal intensity decay in white matter than gray matter was observed along with the TEs. The white matter regions had higher uT_2 fraction values than gray matter ($10.9\% \pm 1.9\%$ vs. $5.7\% \pm 2.4\%$). The uT_2 value was approximately 0.10 ms in white matter .

Conclusion: The higher uT_2 fraction value in white matter compared to gray matter demonstrated the ability of the proposed sequence to capture rapidly decaying signals.

KEYWORDS
k-space, microstructure, non-Cartesian, rosette trajectory, ultra-short echo time

1 | INTRODUCTION

Conventional ^{1}H-MRI sequences are widely used for in vivo imaging, which focus on detecting signals from tissues with relatively long transverse relaxation time (T_2). However, depending on the surrounding chemical environment, some protons in specific tissues in the human body have an ultra-short T_2 (uT_2), which conventional MRI can hardly detect due to their relatively long TEs, on the order of milliseconds (ms). For example, the myelin bilayer in cerebral white matter (WM),[1] cortical and trabecular bones,[2] ligaments,[3] and tissues with high iron concentration[4] have uT_2 values. On the other

hand, UTE MRI[5] sequences are capable of acquiring data with TEs on the order of microseconds (μs), which can provide images of tissues with uT$_2$ directly.

For UTE sequences, the readout gradients are applied immediately after the completion of the RF pulses. Therefore, to achieve the minimum possible TE, each data acquisition in UTE sequences needs to follow a center-out trajectory. Although 2D UTE methods are available, they have limitations making it difficult to achieve an appropriate slice selection and a minimum TE due to eddy currents and imperfect gradients.[6,7] While some advanced techniques overcome the problems of 2D UTE,[8] the most common k-space trajectory used in UTE MRI applications is a 3D radial center-out readout. However, sampling the outer k-space with a radial pattern may not be efficient.[9] Therefore, novel 3D k-space trajectories with greater curvature per spoke have been proposed for a more efficient sampling strategy, e.g., the spiral-like extended cones sampling.[9,10] Other state-of-the-art 3D UTE techniques include density-adapted 3D radial UTE,[11] Fermat looped, orthogonally encoded trajectories UTE sequence[12] and a 3D koosh ball trajectory UTE sequence.[13] Rosette k-space trajectories, which allow a center-out sampling pattern while providing more samples in the outer k-space per spoke than radial trajectories, are also potential candidates for 3D UTE MRI. In addition, the rosette k-space trajectory samples data in a more incoherent pattern than radial trajectories. Therefore, it offers the potential for further acceleration using higher under-sampling factors and compressed sensing (CS) technique for reconstruction.[14] However, 3D rosette k-space patterns have not yet been demonstrated in UTE applications.

Alternatively, a similar MRI-based technique, zero TE (ZTE) MRI, has also been proposed for imaging uT$_2$ tissue. However, unlike UTE imaging, the readout gradients are applied before the RF pulse and are always on in ZTE sequences.[15] In addition, the center k-space in the ZTE sequence is empty because of the dead time due to the switching from RF pulse excitation to data receiving,[15] which requires additional scans or interpolation based on an over-sampling strategy to fill in the missing k-space.[16] Nevertheless, a recent comparison study has shown that UTE and ZTE MRI sequences provide similar image quality and SNR.[17]

One exciting application of 3D UTE and ZTE sequences is in imaging of the myelin bilayer in brain WM. Myelin constituents are water and dry mass, in which the dry mass is composed of about 80% lipids and 20% protein.[18] Since transverse relaxation of the lipid proton signal becomes shorter in this geometrically restricted environment, T$_2$ values vary from a few microseconds to milliseconds, where 75% of the myelin lipid signal manifests T$_2$ values below 100 μs.[19] Thus, conventional MRI sequences with TEs in the order of milliseconds or longer can hardly capture the rapid signal decay of the lipid bilayer.

Many alternative MRI-based methods have been proposed for myelin imaging, e.g., methods based on magnetization transfer effects, separation of myelin water signals, susceptibility imaging, and cortical myelin mapping.[20–23] However, while those methods provide an indirect measurement of myelin, UTE MRI can measure uT$_2$ components of myelin, which may be more specific and more precise.[10,24]

UTE MRI methods have shown great promise for imaging the signals arising from the phospholipid chains of myelin sheaths. Common techniques for the separation of myelin signals based on UTE acquisitions are the combination of inversion recovery suppression[1] and dual-echo subtraction.[25] Even though those methods showed the potential to suppress signals originating from long-T$_2$ components in both gray matter (GM) and WM, the inversion time of inversion recovery suppression is difficult to choose because of the wide range of longitudinal relaxation time (T$_1$) reported in WM (700 to 1100 ms at 3T).[26,27] An alternative method to quantify uT$_2$ components was using a dual-exponential model fitting with data input based on a multiple TE acquisition, ranging from microseconds to milliseconds.[28]

This study aims to develop a novel rosette k-space pattern for 3D UTE MRI and assess the sequence by directly and non-invasively measuring the uT$_2$ components of whole-brain. With the novel k-space design, dual-echo data are sampled in a single acquisition, allowing an extended TE coverage for the dual-exponential complex model fitting. In addition, CS and low-rank denoising were applied to reconstruct images from the acquired non-Cartesian k-space data.

2 | THEORY

Rosettes are non-Cartesian k-space trajectories with high design flexibility.[29] The rosette trajectories are well known for the multiple crossings of k-space origin,[30] which suggests the potential for multiple-echo acquisition.

The following equations define the 3D rosette k-space trajectory[31]:

$$K_{xy}(t) = Kx(t) + i * Ky(t)$$
$$= (K\max * \cos(\varphi)) * \sin(\omega_1 * t) * e^{i\omega_2 t + \beta} \quad (1)$$

$$K_z(t) = (K\max * \sin(\varphi)) * \sin(\omega_1 * t) \quad (2)$$

where $K\max$ is the maximum extent of k-space, ω_1 is the frequency of oscillation in the radial direction, ω_2 is the frequency of rotation in the angular direction, φ determines

the location in the z-axis, and β determines the initial phase in the angular direction.

In Figure 1A, a rosette trajectory is shown for the specific case where ω_1 and ω_2 are set to be equal. The origin of the k-space is sampled at the beginning and the end of each TR, forming a petal-like sampling pattern (Figure 1A). Dual-echo images can be generated within a single acquisition with a manual separation at the middle of each data readout (Figure 1A,B). TE values are separately determined by the time of two crossings of the k-space origin. The gradients of one petal trajectory are shown in Figure 1B. A specific gradient ramp-up was used to keep the overall rosette shape (Supporting Information Figure S1, which is available online), which resulted in oversampling at the center k-space. The ADC (analog to digital converter) was turned on during this gradient ramp-up period to enable the shortest possible TE (details in Section 5). The separate k-space trajectories in the x, y, and z directions are also shown in Figure 1B.

The influence of the value of ω_1 and ω_2 is mainly on the speed of trajectory. For the dual-echo acquisition, at the end of the readout duration, the trajectory needs to be located at the exact k-space origin, which requires:

$$\omega_1 * \text{samples per petal} * \text{dwell time} = \pi \qquad (3)$$

where dwell time is 10 μs. In this study, ignoring the oversampling, 195 samples per petal were acquired (210 samples counting the oversampling). The parameters $\omega_1 = \omega_2$ are then calculated as:

$$\omega_1 = \omega_2 = \frac{\pi}{195 * 10} * 1000 = 1.611 \text{ kHz.} \qquad (4)$$

The other parameters for the UTE acquisition with $2 \times 2 \times 2 \text{ mm}^3$ spatial resolution were: $K\max = 250$ m, number of total petals = 36100, samples per petal = 210, φ was sampled uniformly in the range of $(-\pi/2, \pi/2)$, and β was sampled uniformly in the range of $(0, 2\pi)$. With 10 μs readout dwell time, the difference between first TE (TE$_1$) and second TE (TE$_2$) is equal to $210 \times 10 \ \mu s = 2.1$ ms (other scan parameters are stated in the Section 3). Based on Nyquist criteria calculation, to avoid artifacts, the minimum number of total petals should be $4\pi * r^2 \approx 45239$, where r represents half of the 1D matrix size ($r = 60$ in this paper). Due to the 3D rosette k-space pattern (i.e., the curvature and k-space coverage), this 80% (36 100/45 000) undersampling pattern did not suffer significant artifacts. The noise generated by the undersampling strategy was primarily removed by CS reconstruction. Because of these reasons, the trajectory with 36 100 petals is considered to be a fully sampled k-space for the purpose of this study. The Nyquist criteria for samples per petal varied depending on ϕ and β. It reaches the maximum required

samples when $\phi = 0$, which is $\pi * r = 189$ samples per petal (the number is for two TEs). Crusher gradients in all three directions were applied at the end of each readout gradient (not shown in Figure 1B).

The 3D radius (including all x, y, and z directions) of the rosette trajectory is expressed with a sine function ($K\max * \sin(\omega_1 * t)$), which varies within $(0, K\max)$. In addition, the 3D radius of the rosette trajectory has a fast rate of change at small radii of k-space but a slow velocity at large radii of k-space. With the constant readout dwell time, the k-space velocity difference led to increased samples with the radii of k-space for each readout spoke (about 43% of samples at radii of k-space larger than $0.75K\max$). However, for each readout spoke, the 3D radius of the standard radial trajectory has a constant rate of change, which led to a uniform sampling with the 1D radii of k-space (25% samples at radii of k-space larger than $0.75Kmax$). A 2D example is illustrated in Figure 1C.

3 | METHODS

For quantitative comparison of the sampling trajectories, the shift-invariant point spread functions (PSFs) of full rosette k-space patterns (first and second echoes), half undersampled rosette k-space pattern, and 3D radial acquisition with golden angle, were calculated with a fast Fourier transform based method.[32]

The study was approved by the Institutional Review Boards of Purdue University. Five healthy subjects underwent brain scans with a whole-body 3T MRI system (Prisma, Siemens, Erlangen, Germany), with a maximum gradient amplitude of 80 mT/m and maximum slew rate of 200 mT/m/ms isotropically. A vendor-supplied 20-channel receiver head coil was used for all volunteers. An magnetization-prepared rapid gradient-echo (MPRAGE) sequence was performed before the UTE sequence for the anatomical reference. The parameters used in the dual-echo 3D UTE sequence with rosette k-space sampling were: Field of view = 240 x 240 x 240 mm^3, matrix size = 120 x 120 x 120, readout dwell time = 10 μs, flip angle = 7-degree, TR = 7 ms, readout duration = 2.1 ms, and RF pulse duration = 10 μs. Ten repeated dual-echo UTE scans were performed with varied TEs. The first TEs were 20, 40, 60, 80, 100, 150, 300, 600 μs; 1 and 1.5 ms. The second TEs were 2.12, 2.14, 2.16, 2.18, 2.2, 2.25, 2.4, 2.7, 3.1, and 3.6 ms. For one dual-echo UTE acquisition, 36 100 petals were acquired (full k-space acquisition without acceleration), resulting in a scan duration of 4.2 min (36 100 x 7 ms). The 10 repeated UTE scans lasted 42 min, and the total scan time was about 50 min for each volunteer.
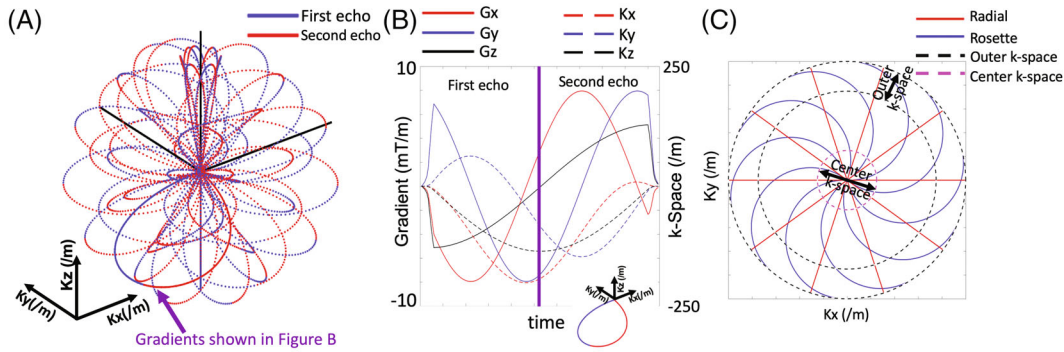
FIGURE 1 Illustrations of the 3D rosette k-space design. A, Selective spokes with varied rotations in the k_x–k_y plane and varied extensions in the k_z-axis are shown. Each spoke crosses the origin of k-space at the beginning and end, forming a "petal-like" pattern. The dual-echo acquisition (blue: first echo, red: second echo) was generated based on manual separation at the middle of each "petal-like" pattern. B, The gradients in all three directions (red: gradients in the x-axis, Gx; blue: gradients in the y-axis, Gy; black: gradients in the z-axis, Gz) of a selective spoke as shown in Figure 1A. The separated k_x, k_y, and k_z curves are also shown in Figure 1B (red dash line: k_x; blue dash line: k_y; black dash line: k_z). All gradients began at zero amplitude to avoid any potential delays caused by the gradients' ramp-up. C, A 2D example to illustrate the differences between rosette (blue) and radial (red) acquisitions in peripheral (outer) k-space coverage (regions between black dash lines). With greater curvature, rosette trajectory provides more samples in the peripheral k-space than radial trajectory

Image reconstruction and post-processing steps were performed in MATLAB (MathWorks, USA). The nonuniform fast Fourier transform was used to calculate the forward encoding transform of the acquired k-space data.[33] A CS approach was used for image reconstruction, using total generalized variation as the sparsifying penalty.[34] The complex-valued coil sensitivity maps were first extracted from the center of k-space using ESPIRIT for coil combination.[35] Then, the reconstructed complex image data were combined for each TE and resulted in the magnitude image data.

The post-processing procedure was performed using FMRIB Software Library and Statistical Parametric Mapping software. The workflow of post-processing steps was summarized in Figure 2, including registration to T_1-weighted anatomy images,[36,37] brain tissue extraction,[38] bias-field correction,[39] voxel-wised LORA (low-rank approximations) correction to reduce spurious fluctuations while preserving the relevant signal decays,[40] and voxel-wised dual-exponential fitting based on the magnitude of the free induction decay signal. Ten dual-echo UTE acquisitions allow to use additional 10 second TEs in the model for dual-exponential fitting. The fitting model was expressed as the equation[28,41]:

$$S(\text{TE}) = S_{0,\text{short}} \exp\left(-\frac{\text{TE}}{T^*_{2\text{short}}}\right) * \exp\left(2\pi\Delta f_{\text{short}}\text{TE}\right) \dots$$
$$+ S_{0,\text{long}} \exp\left(-\frac{\text{TE}}{T^*_{2\text{long}}}\right) * \exp\left(2\pi\Delta f_{\text{long}}\text{TE}\right) \quad (5)$$

where $S_{0,\text{short}}$ and $S_{0,\text{long}}$ are the proton density, and Δf_{short} and Δf_{long} are the frequency shift with short $T^*_2(T^*_{2\text{short}})$,

and long $T^*_2\left(T^*_{2\text{long}}\right)$, respectively. After the fitting, the voxel-wised ratio between $S_{0,\text{short}}$ and the total proton density $\left(S_{0,\text{short}} + S_{0,\text{long}}\right)$ was reported as uT$_2$ fraction map, and $T^*_{2\text{short}}$ and $T^*_{2\text{long}}$ were reported as uT$_2$ value and long-T$_2$ value maps. All maps were registered to a standard brain atlas (MNI-152) for better visualization and then were averaged across subjects for statistical analysis. The uT$_2$ fractions in total WM and total GM were reported individually and as mean across subjects. A two-sample t-test was used to test whether the uT$_2$ fractions were statistically different between GM and WM. In addition, the uT$_2$ fractions were quantified based on selected regions of interest (ROIs), including cingulum, corona radiata, internal capsule, corpus callosum, external capsule, fornix, and sagittal stratum.

A phantom and one volunteer were scanned using the dual-echo 3D rosette UTE sequence and a 3D radial UTE sequence with golden angle acquisition[42] to compare the image quality after reconstruction. For this comparison, most of the imaging parameters were identical or the closest possible values between the two sequences, which were: Number of spokes (petals) = 36 100, TE$_{\text{rosette}}$ = 20 μs, TE$_{\text{radial}}$ = 30 μs, TR = 7 ms, flip angle = 7-degree, field of view = 240 × 240 × 240 mm^3, matrix size = 128 × 128 × 128, readout dwell time = 10 μs, and RF pulse duration = 10 μs. For the dual-echo 3D rosette UTE sequence, 105 samples were acquired per petal per TE, while 128 samples were acquired per spoke for 3D radial UTE. Two reconstruction methods were performed: CS (as described above) and regular regridding applying a density compensated adjoint nonuniform fast Fourier transform. The reconstruction processing steps were kept identical for the data
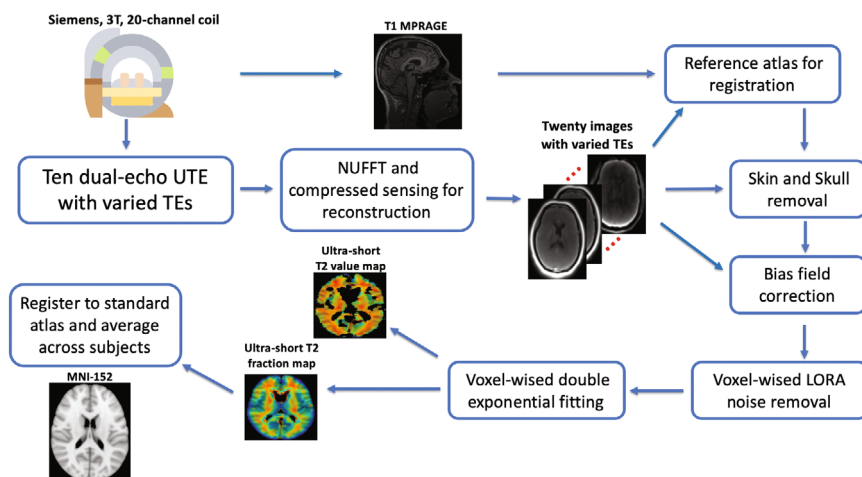
acquired by both the dual-echo 3D rosette and radial UTE sequences. In addition, a Cartesian-based fast low angle shot (FLASH) sequence was performed for comparison to evaluate the image quality (imaging parameters for phantom: Spatial resolution $= 2 \times 2 \times 2 \, mm^3$, matrix size $= 128 \times 128 \times 56$, TE $= 2.77$ ms, TR $= 7$ ms, flip angle $= 7$-degree, imaging parameters for in vivo: Spatial resolution $= 2 \times 2 \times 2 \, mm^3$, matrix size $= 128 \times 128 \times 128$, TE $= 2.59$ ms, TR $= 7$ ms, flip angle $= 4$-degree). The SNRs were calculated based on the mean signal intensities of the ROIs over the SD of the signal intensities in three background ROIs. In addition, image quality was assessed by the structural similarity index to the reference image acquired by the FLASH sequence.

4 | RESULTS

The trajectory PSFs with dB unit are shown in Figure 3. The full rosette k-space patterns (first and second echoes) have the highest PSF peak value, which is around −1.15 dB, and a full width at half maximum at (2.23, 2.23, 2.23 mm). In contrast, the half undersampled rosette k-space pattern suffers further signal loss to have PSF peak value around −1.58 dB, and a full width at half maximum at (2.20, 2.20, 2.30 mm). The radial UTE with golden angle acquisition (same number of spokes compared to full rosette pattern) has the PSF peak value in between, which is −1.37 dB, and a full width at half maximum at (2.19, 2.19, 2.31 mm).

Figure 4 (phantom) and Supporting Information Figure S2 (in vivo) compare the dual-echo 3D rosette UTE sequence and the 3D radial UTE sequence. All the reconstructed images were normalized to have signal intensity ranging from 0 to 1. The standard regridding reconstruction method resulted in "ringing" artifacts for both acquisition methods (as shown in Figure 4B,D,F

and Supporting Information Figure S2B,D,F), which had been minimized by the CS reconstruction method (as shown in Figure 4A,C,E and Supporting Information Figure S2A,C,E correspondingly). The reconstructed image quality by the dual-echo 3D rosette UTE sequence was overall better than the 3D radial UTE, in terms of SNR (as shown in Figure 4A vs. 4E, and Supporting Information Figure S2A vs. S2E), and the ability to capture additional structural information (white dots as shown in Figure 4A, but not shown in Figure 4E). In addition, the dual-echo 3D rosette sequence detected the rapid decaying signals originating from the foam pad used for positioning (Supporting Information Figure S3). However, the foam pad was not identified by the 3D radial sequence.

The results of the ROI-based quantitative comparison are shown in Figure 5. The ROIs of phantom and in vivo images (reconstructed by regridding) were selected arbitrarily (red rectangular in Figure 5). The 3D rosette k-space pattern reports higher SNR than 3D radial UTE acquisition with golden angle, based on phantom scans (rosette first TE: 315, rosette second TE: 211, vs. radial: 40) and in vivo scans (rosette first TE: 137, rosette second TE: 113, vs. radial: 43). The 3D rosette k-space pattern has slightly higher similarity to the FLASH images than the 3D radial, based on both phantom scans (rosette first TE: 0.89, rosette second TE: 0.87, vs. radial: 0.86) and in vivo scans (rosette first TE: 0.72, rosette second TE: 0.66, vs. radial: 0.65).

In Figure 6A, brain image slices from a volunteer are shown for five representative TEs, 20 μs, 100 μs, 2.12 ms, 2.4 ms, and 3.6 ms. There was little or no contrast between WM and GM at the minimum UTE (TE = 20 μs), whereas the contrast between WM and GM increased at longer TE, as expected.

Figure 6B shows the differences in signal decay between WM ROI (blue) and GM ROI (red). The signal intensities with different TEs were normalized based on the detected signal at the shortest TE of 20 μs. WM and GM
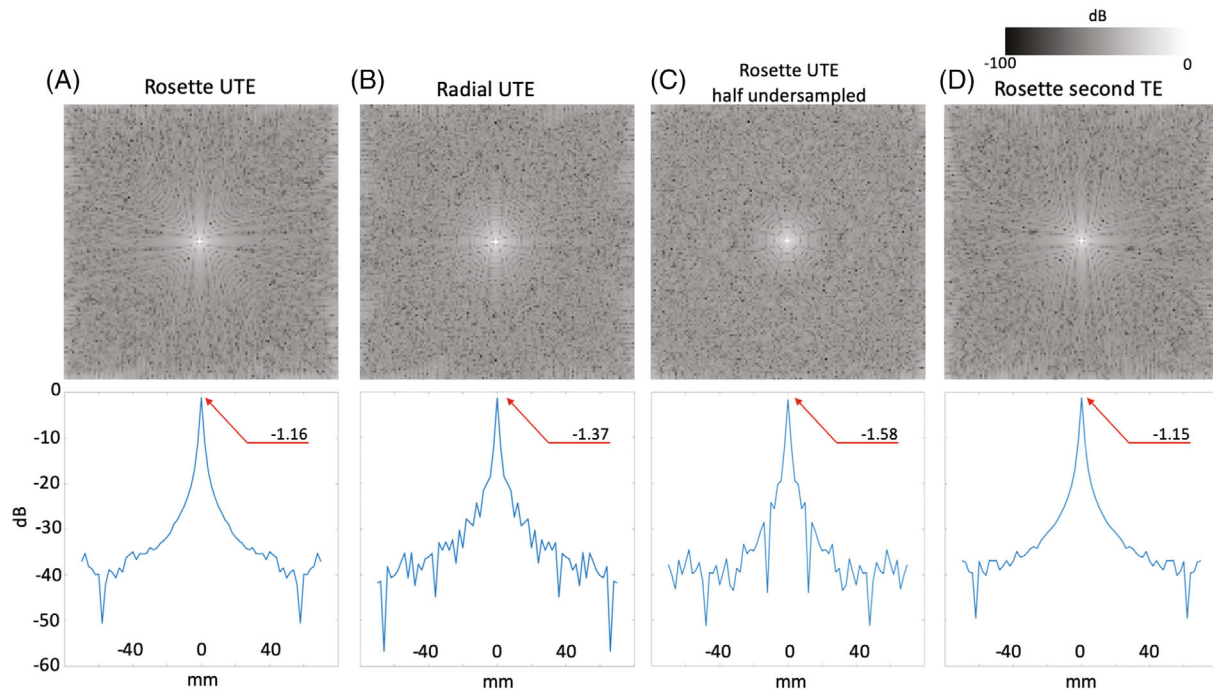
FIGURE 3 Point spread function (PSF) comparison among different k-space designs. The top figures represented the center slice in x–y plane of the 3D PSF. The bottom figures showed the center line in x-axis (-70 to 70 mm) of the top figures. All results were converted into dB units to illustrate signal loss. The peak values of the PSF were also identified in the bottom figures. A, Rosette first echo k-space trajectory. B, Radial UTE k-space trajectory with golden angle acquisition. C, Rosette first echo k-space trajectory with undersample factor = 2. D, Rosette second echo k-space trajectory

signal decay curves showed fast signal drop at UTE period (below 0.15 ms), which was about 5% in selected WM ROI and about 4% in GM ROI. The signal curve of WM ROI continued to drop (about 15% at TE = 3.6 ms), while the signal curve of GM ROI had a slower decay at longer TEs (about 10% at TE = 3.6 ms).

Table 1 summarizes the uT_2 fraction, uT_2 values, and long-T_2 values in total GM and total WM individually and as mean across subjects. The voxels containing fitting results of uT_2 values longer than 1 ms were identified as outliers and excluded (portion of outliers: 0%–5% in WM, 3%–15% in GM). All subjects and the average indicated a significantly higher uT_2 fraction in WM than GM ($P < 0.0001$ for all subjects and the mean). The average WM uT_2 fraction across subjects was $10.9\% \pm 1.9\%$, and the average GM uT_2 fraction across subjects was $5.7\% \pm 2.4\%$. In addition, the average WM uT_2 value was 0.10 ± 0.06 ms, and the average WM long-T_2 value was 54 ± 18 ms. In contrast, the average GM uT_2 value was 0.09 ± 0.12 ms, and the average GM long-T_2 value was 57 ± 21 ms.

Figure 7 shows the mean uT_2 fraction map (Figure 7A), the mean uT_2 value map (Figure 7B), and the mean long-T_2 value map (Figure 7C) in MNI-152 space. The uT_2 fraction map (Figure 7A) indicated a generally homogeneous uT_2 fraction among voxels in WM, which was higher than the uT_2 fraction among voxels in GM. A generally slightly faster uT_2 value was observed in GM than in WM. The

long-T_2 component value map indicated an increased T_2 value across GM and the CSF compared to the WM, which is in line with previous reports.[28,43] (The uT_2 fraction and uT_2 value maps from two subjects are shown in Supporting Information Figure S4). The mean frequency shift ($\Delta f_{short} - \Delta f_{long}$) map is shown in Supporting Information Figure S5. A significant difference in frequency shift is observed between WM (around -5 to -40 Hz) and GM (around -150 to -200 Hz).

Figure 8 summarizes the mean and SD of the uT_2 fraction among different ROIs across five subjects (cingulum, corona radiata, internal capsule, corpus callosum, external capsule, fornix, and sagittal stratum). The ROI locations are indicated on the left and right sides of Figure 8. All the ROIs were identified as WM-rich regions and reported about 10% as the uT_2 fraction. The lowest reported ROI-based uT_2 fraction value, $9.4\% \pm 1.0\%$, was in the corpus callosum. The highest reported ROI-based uT_2 fraction value, $12.2\% \pm 1.6\%$, was in the fornix.

5 | DISCUSSION

This study developed a novel 3D dual-echo UTE sequence based on a rosette k-space trajectory. The advantages of this novel design included: (1) increased sampling density in the outer k-space, (2) improved PSF and SNR compared
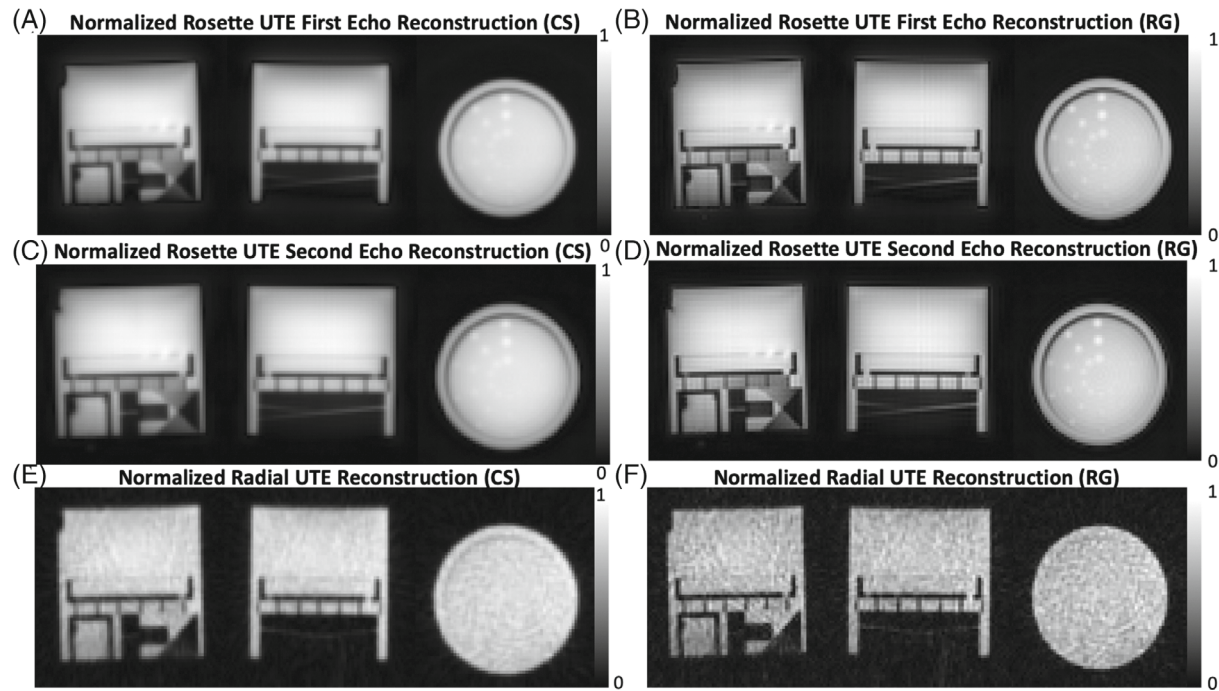
FIGURE 4 Phantom performance comparison between UTE sequences with 3D dual-echo rosette trajectory and 3D radial golden angle trajectory. All the images were normalized to have signal intensity from 0 to 1. A, C, E, Reconstructed images based on compressed sensing (CS) technique from data sampled by the first echo of rosette trajectory (A), the second echo of rosette trajectory (C), and radial trajectory (E). B, D, F, Reconstructed images based on regridding (RG) technique from data sampled by the first echo of rosette trajectory (B), the second echo of rosette trajectory (D), and radial trajectory (F)

TABLE 1 Individual and mean across subjects ultra-short T_2 fractions, ultra-short T_2 values, and long T_2 values in total white matter (WM) and total grey matter (GM). All values are shown as mean $\pm$ standard deviation. The voxels containing fitting results of uT_2 values longer than 1 ms were excluded. A two-sample t-test was used to test whether the ultra-short T_2 fractions were statistically different between GM and WM, which P-values were calculated

Subject number	uT_2 fractions			uT_2 values		Long T_2 values	
	Total GM	Total WM	P-values	Total GM	Total WM	Total GM	Total WM
1	$7.5\% \pm 1.1\%$	$11.6\% \pm 0.9\%$	<0.0001	0.07 ± 0.10	0.07 ± 0.02	66 ± 17	54 ± 13
2	$3.7\% \pm 1.4\%$	$9.9\% \pm 1.3\%$	<0.0001	0.09 ± 0.16	0.07 ± 0.10	45 ± 19	43 ± 18
3	$3.9\% \pm 2.1\%$	$9.1\% \pm 1.0\%$	<0.0001	0.09 ± 0.08	0.09 ± 0.04	71 ± 15	67 ± 13
4	$8.7\% \pm 1.4\%$	$13.8\% \pm 1.2\%$	<0.0001	0.10 ± 0.08	0.12 ± 0.03	74 ± 13	64 ± 13
5	$5.4\% \pm 1.6\%$	$10.5\% \pm 1.1\%$	<0.0001	0.10 ± 0.11	0.11 ± 0.06	43 ± 14	38 ± 9
Total	$5.7\% \pm 2.4\%$	$10.9\% \pm 1.9\%$	<0.0001	0.09 ± 0.12	0.10 ± 0.06	57 ± 21	54 ± 18

to radial acquisition, (3) a smooth transition (zero-delay) between the two echoes of dual-echo acquisition. As a result, a statistically significantly higher uT_2 fraction value was found in WM compared to GM. In addition, the uT_2 fraction value was homogeneously distributed among WM voxels.

The achievement of the shortest TE in UTE sequences is limited by the system hardware, not only by the dead time[15] but also by the slew rate limitation if the initial gradient amplitude is high in any direction. In this 3D rosette k-space design, a specific gradient ramp-up was used to maintain the overall rosette shape. In the meantime, the ADC was turned on during ramp-up time to provide UTE. The strategy was to gradually increase the ω_1 and ω_2 to the designed value of 1.611 kHz at the beginning of each TR. With this strategy, the maximum slew rate was about 140 mT/m/ms for all three directions separately. In addition, the initial
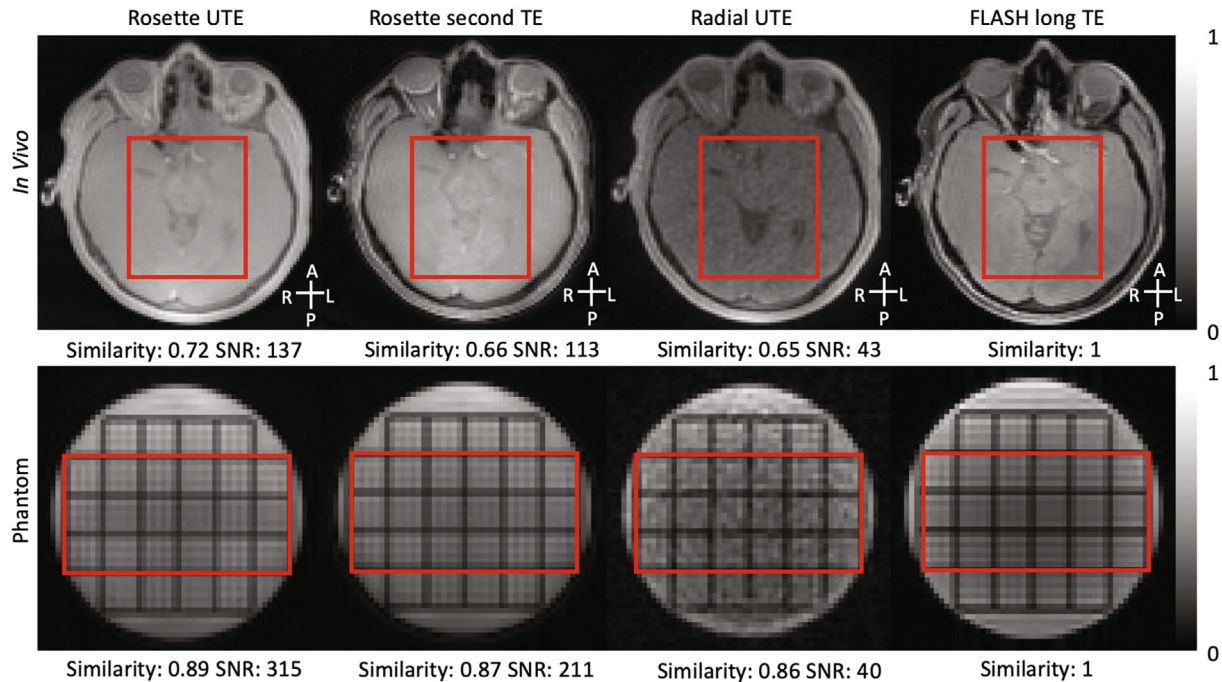
FIGURE 5 Quantitative performance comparison between UTE sequences with 3D dual-echo rosette trajectory and 3D radial golden angle trajectory. All the images were normalized to have signal intensity from 0 to 1. The similarity was evaluated based on the ROI (red rectangular), using the structural similarity index with images acquired by the Cartesian FLASH sequence as reference. The SNR was calculated based on the mean signal intensity inside the ROI over the SD of the background (not shown in the Figure). A, anterior; L, left; P, posterior; R, right; FLASH, fast low angle shot.

sampled data still followed the originally designed rosette trajectory, which was used for image reconstruction. This resulted in an over-sampling at the center k-space (about 20% of samples located in radii of k-space smaller than $0.25K$ max), which could improve the SNR. Similar to ZTE applications, this study used a small flip angle (7-degree). Although large flip angles are allowed in UTE acquisition, a small flip angle could minimize the T_1 influence on the detected signals.[44]

The volume of the 3D k-space is proportional to the cube of the radius of the acquired k-space. The volume of radii larger than $0.75K$ max (considered as peripheral k-space) occupied about 58% ($= [1^3 - 0.75^3]/1^3$) of the entire volume of 3D k-space with the radius of K max. However, the volume of radii smaller than $0.25K$ max (considered as center k-space) only occupied about 2% ($= 0.25^3/1^3$) of the entire volume of k-space. This resulted in a much larger peripheral k-space than the center k-space volume in 3D cases. Therefore, the conventional radial acquisition, which samples uniformly along with the 1D radius of k-space (25% of samples at center k-space, and 25% of samples at peripheral k-space), may not be efficient at the large radii of 3D k-space. Under the specific circumstances, e.g., 80% undersampling number of spokes, the PSF analysis demonstrated that the 3D radial acquisition suffered more noise with a lower peak value

than the 3D dual-echo rosette trajectory. The reconstructed images acquired by the 3D radial pattern confirmed that disadvantage, which resulted in noise amplification and the loss of structural details. In addition to the insufficient samples at the large radii of 3D k-space, the suboptimal imaging parameters, such as the insufficient number of spokes and long TR set to match 3D dual-echo rosette UTE, further contributed to the degraded performance of 3D radial acquisition. The structural similarity index indicated a higher value of phantom images (around 0.9) than in vivo images (around 0.7), compared to the reference acquired by the Cartesian FLASH sequence. This may be because the contrast of in vivo images is highly related to the imaging parameters, including TE, TR, and flip angle. However, the inner plastic gridding mainly determines the contrast of phantom images.

The newly proposed 3D rosette trajectory has increased samples at larger radii of k-space, which provides greater sampling density in peripheral k-space. The advantages of the newly proposed 3D rosette trajectory (i.e., trajectory curvature and k-space coverage) may have the potential for further acceleration by acquiring fewer petals without losing image quality. As stated in the Theory section, the number of petals (spokes) used to compare the dual-echo 3D rosette and the 3D radial trajectories is an 80%
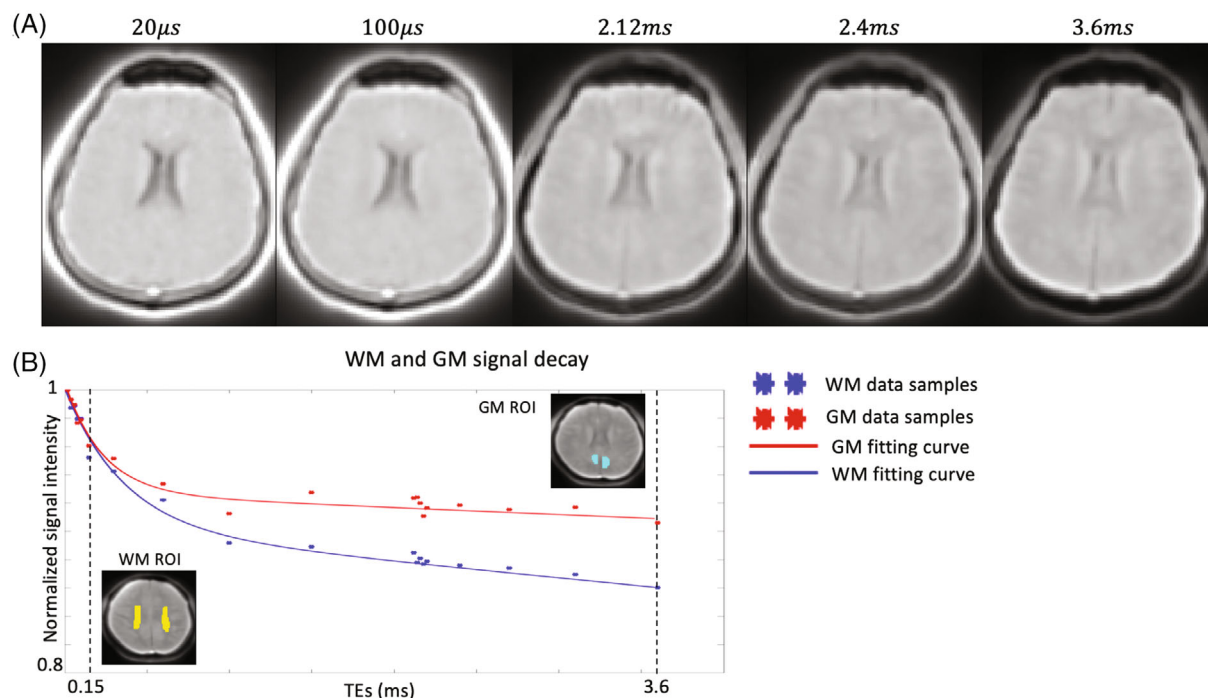
FIGURE 6 A, Five brain image slices with 20 µs, 100 µs, 2.1 ms, 2.4 ms, and 3.6 ms TEs from a volunteer are shown. B, Signal decay curves from selected ROIs, which are identified as white matter (WM) ROI (left bottom corner) and gray matter (GM) ROI (right upper corner). All signals were normalized based on the shortest TE (~20 µs). The stars showed the distribution of signals with different TEs from WM ROI (blue) and GM ROI (red). Black dash lines were used to identify the UTE region (below 0.15 ms). The fitting results of WM ROI: uT_2 fraction = 13.0%, uT_2 value = 0.13 ms, long T_2 value = 60.9 ms. The fitting results of GM ROI: uT_2 fraction = 8.7%, uT_2 value = 0.09 ms, long T_2 value = 74.9 ms

undersampling pattern. However, using the CS reconstruction, the reconstructed dual-echo 3D rosette images did not suffer from significant artifacts. They did not lose structural information compared to the images acquired by the 3D radial scan. In addition, although the regridding method resulted in sharper images, they suffered from "ringing" artifacts, which could be caused by gradient imperfections or sampling density compensation. In this study, the CS reconstruction was tuned to minimize the "ringing" artifact, with the cost of some loss of effective spatial resolution. Adapting this dual-echo 3D rosette trajectory to retain image quality with an undersampling strategy may lead to future directions. For example, with an additional undersampling factor = 2 (40%) or 4 (20%), the total scan time of the 10 dual-echo UTE sequences can be shortened to between 21 and 10 min, which could be acceptable in clinical settings (reconstructed images with undersampling factor = 2 were tested for further acceleration purpose and are shown in Supporting Information Figure S6).

Instead of combining inversion recovery suppression and dual-echo subtraction,[10] dual-exponential complex fitting was performed in this study, offering uT_2 fraction and uT_2 value maps. Although the quantitative analysis of the uT_2 fraction and value maps still needs validation,[10]

this method showed a potential way to compare across subjects. The setback of this method was the need for a multiple TEs acquisition, which increased total scan time. However, with the dual-echo rosette sequence proposed in this study, 20 images with different TEs could be acquired in a reasonable total scan time. A clinically acceptable scan time can be achieved by further reducing acquisition duration with an undersampling strategy. Some publications used a three-component exponential model with an additional intermediate T_2 range of around 10 ms for regression.[28] This model might be more accurate. However, it significantly increases the unknown parameters that need to be estimated. The current TE samples may not support a fitting with a three-component model, as the fitting results within some voxels were already unreliable with the current two-component exponential model. In addition, a series of TEs in a wider range (i.e., including TE at 10 ms) may better describe the free induction decay curve of the long-T_2 component. However, including TE at 10 ms will significantly increase TR (longest TE = 3.6 ms and TR = 7 ms in this study), which correspondingly increases the total scan time.

Overall, the results of uT_2 components quantification, acquired by the dual-echo 3D rosette sequence, agree with

FIGURE 7 The results of dual-exponential fitting: the mean ultra-short T$_2$ components (uT$_2$) fraction map (A), the mean uT$_2$ value map (B), the long T$_2$ value map (C). Please note that some voxels were black in Figure 7B (primarily located in cerebrospinal fluid and gray matter), caused by high uT$_2$ values reaching the top threshold of the color bar. A, anterior; L, left; P, posterior; R, right;
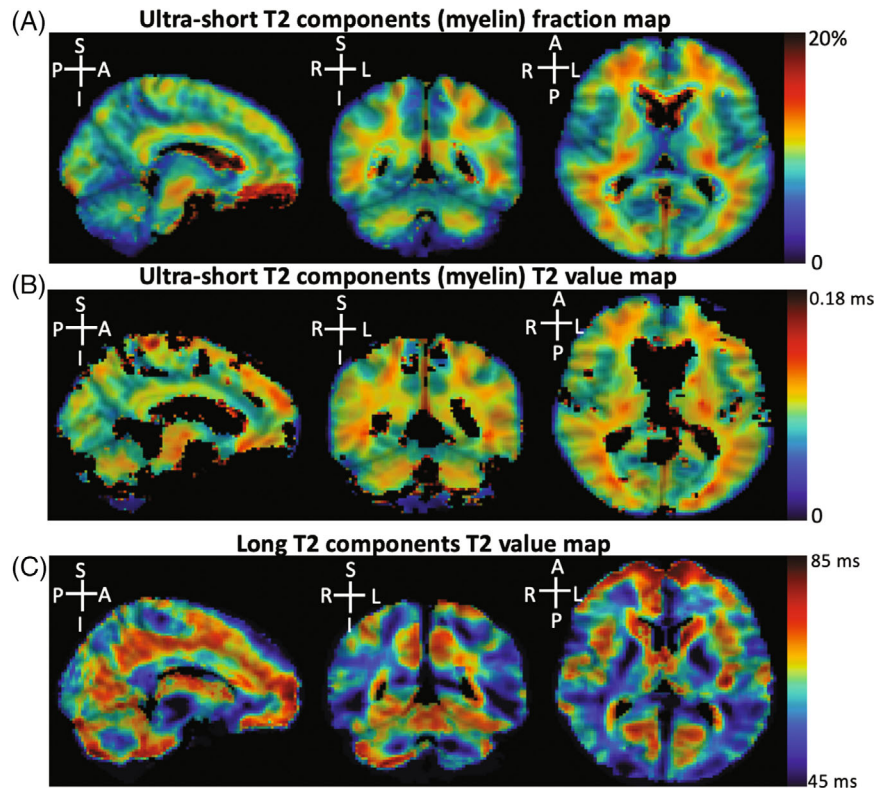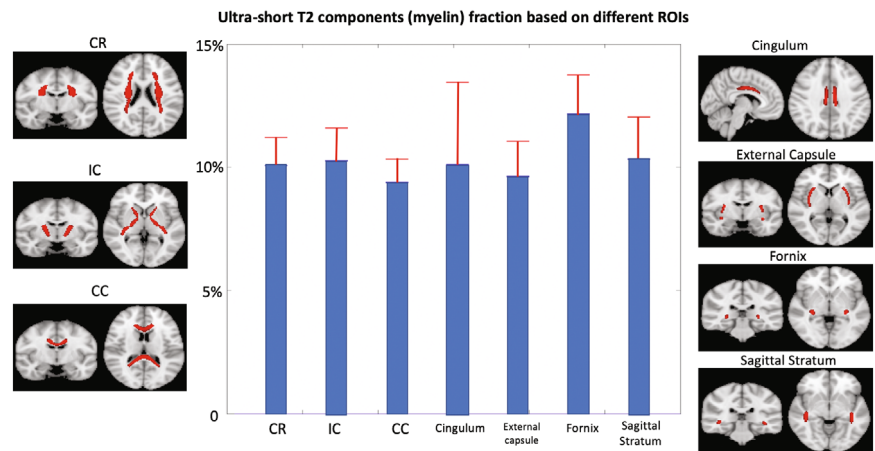

FIGURE 8 The mean (blue columns) and SD (red) of ultra-short T$_2$ components (uT$_2$) fraction among different ROIs across subjects, quantified based on the five individual uT$_2$ fraction maps. The locations of the ROIs are indicated on the left and right sides of the image. CC, corpus callosum; CR, corona radiata; IC, internal capsule

previous publications with 3D radial or 3D cones trajectories.[10,45] First, little or no contrast at short TEs (i.e., below 100 µs) was achieved without IR suppression. Second, larger signal decay in WM than in GM was observed, which increases the contrast between WM and GM at longer TEs. Third, the uT$_2$ components were mainly distributed in WM voxels, resulting in a generally higher uT$_2$ fraction value in WM compared to GM. Additionally, the uT$_2$ fraction values based on ROIs aligned with previous publications,[46–48] around 10% to 12% in most WM-rich brain regions.

One disadvantage of the 3D rosette k-space pattern is that more samples per acquisition were needed (1.5 times more samples than radial). In addition, the long readout

duration of this rosette trajectory (2.1 ms for dual-echo acquisition, which means 1.05 ms for the first echo acquisition) may suffer image blurring caused by the fast signal decay.[6] A previous study has shown that the ideal sampling duration is 0.81*T$_2$ of the imaging tissue for radial UTE.[49] However, such a short sampling duration would result in spatial resolution loss because not enough samples would be acquired.[6] Therefore, the sampling duration of two to four times T$_2$ of the imaging tissue was typically used.[6] For the myelin imaging applications, the sampling duration was usually set to 0.3 to 1 ms.[1,25,50]

One of the significant issues of model-based processing is to fit a large number of parameters, long and ultra-short signal decay rates, and respective frequency shifts. This

results in complications with the degradation of the accuracy and precision of the parameter estimations. Although stable frequency differences between WM and GM were observed,[51] the frequency shift values may not be reliable because this study used magnitude data for the complex model. On the other hand, we attempted to use the complex data for the complex model.[28] However, the estimations hit the boundary conditions and resulted in unstable and hence inhomogeneous estimates of parameters in two out of five subjects (data were not shown). This might be due to the relatively long acquisition duration for both echoes (2.1 ms), propagation of phase errors due to eddy currents, gradient delays, and breathing. One can overcome these limitations using field cameras.[52] Alternatively, the gradient impulse response function can be calculated to mimic the gradient chain's behavior and then used for the image reconstruction retrospectively.[53]

Recent publications showed that the brain iron content led to inaccurate results of the myelin water fraction (about 26%–28% decrease after iron extraction by reductive dissolution of brain slice samples) by myelin water imaging technique.[54] Although 3D UTE rather than myelin water imaging was used in this study, the influence of iron content on the results was not ruled out. The presence of iron increases the magnetic field inhomogeneity, resulting in a shorter T_2^*. As a result, some protons which have relatively long-T_2 may be shortened into the uT_2 range[55] within substantia nigra,[56] putamen,[57] and globus pallidus[58] regions, which have potential age-related iron accumulation. Those regions had high signal intensities in our reconstructed images of the novel dual-echo 3D rosette acquisition with the shortest TE ($\sim20\,\mu s$). A new model for fitting could regress the iron effect out.[59] In addition, quantitative susceptibility mapping[60] may be applied for iron measurement since the proposed sequence allows a dual-echo acquisition.

There are some other limitations of this study. First, the sample pool of five healthy volunteers was limited. Due to its nature as proof of concept, the sensitivity of the novel 3D rosette trajectory UTE sequence and/or the dual-exponential model-fitting method to detect diseased states (e.g., demyelination) is undetermined. A prospective study is required to address this limitation. Second, other macromolecules with similar uT_2 values may contribute to the detected signals.[55] For future studies, patients (and/or animals) with different stages of myelination diseases will be recruited to test the performance of this novel rosette k-space trajectory. In addition, a comparison of the 3D rosette dual-echo UTE sequence to other MRI-based methods, e.g., myelin water imaging and magnetization transfer, is another potential future direction.

In conclusion, this study proposed a novel dual-echo 3D rosette k-space trajectory, specifically for UTE MRI and MR spectroscopic imaging applications.[61,62] The higher uT_2 fraction value found in WM compared to GM demonstrated the ability of this sequence to capture rapidly decayed signals. In addition, the fitting based on the dual-exponential model provided quantitative results of the uT_2 fraction, which could be used for myelination assessment in the future.

CONFLICT OF INTEREST
The authors have no conflict of interest to disclose.

ORCID
Xin Shen https://orcid.org/0000-0003-0184-8751
Ali Caglar Özen https://orcid.org/0000-0003-3536-0826
Serhat Ilbey https://orcid.org/0000-0002-3574-4320
Mark Chiew https://orcid.org/0000-0001-6272-8783
Uzay Emir https://orcid.org/0000-0001-5376-0431

TWITTER
Uzay Emir @uzemye

REFERENCES
1. Seifert AC, Li C, Wilhelm MJ, Wehrli SL, Wehrli FW. Towards quantification of myelin by solid-state MRI of the lipid matrix protons. *NeuroImage*. 2017;163:358-367.
2. Jerban S, Ma Y, Wong JH, et al. Ultrashort echo time magnetic resonance imaging (UTE-MRI) of cortical bone correlates well with histomorphometric assessment of bone microstructure. *Bone*. 2019;123:8-17.
3. Fukuda T, Wengler K, Tank D, et al. Abbreviated quantitative UTE imaging in anterior cruciate ligament reconstruction. *BMC Musculoskelet Disord*. 2019;20:426.
4. Doyle EK, Toy K, Valdez B, Chia JM, Coates T, Wood JC. Ultra-short echo time images quantify high liver iron. *Magn Reson Med*. 2018;79:1579-1585.
5. Madio DP, Lowe IJ. Ultra-fast imaging using low flip angles and FIDs. *Magn Reson Med*. 1995;34:525-529.
6. Du J, Bydder M, Takahashi AM, Chung CB. Two-dimensional ultrashort echo time imaging using a spiral trajectory. *Magn Reson Imaging*. 2008;26:304-312.
7. Josan S, Kaye E, Pauly JM, Daniel BL, Pauly KB. Improved half RF slice selectivity in the presence of eddy currents with out-of-slice saturation. *Magn Reson Med*. 2009;61: 1090-1095.

8. Latta P, Starcuk Z Jr, Kojan M, et al. Simple compensation method for improved half-pulse excitation profile with rephasing gradient. *Magn Reson Med*. 2020;84:1796-1805.

9. Wan L, Zhao W, Ma Y, et al. Fast quantitative 3D ultrashort echo time MRI of cortical bone using extended cones sampling. *Magn Reson Med*. 2019;82:225-236.

10. Ma YJ, Searleman AC, Jang H, et al. Whole-brain myelin imaging using 3D double-echo sliding inversion recovery ultrashort echo time (DESIRE UTE) MRI. *Radiology*. 2020;294:362-374.

11. Muller M, Egger N, Sommer S, et al. Direct imaging of white matter ultrashort T2* components at 7 tesla. *Magn Reson Imaging*. 2022;86:107-117.

12. Willmering MM, Robison RK, Wang H, Pipe JG, Woods JC. Implementation of the FLORET UTE sequence for lung imaging. *Magn Reson Med*. 2019;82:1091-1100.

13. Mendes Pereira L, Wech T, Weng AM, et al. UTE-SENCEFUL: first results for 3D high-resolution lung ventilation imaging. *Magn Reson Med*. 2019;81:2464-2473.

14. Li Y, Yang R, Zhang C, Zhang J, Jia S, Zhou Z. Analysis of generalized rosette trajectory for compressed sensing MRI. *Med Phys*. 2015;42:5530-5544.

15. Weiger M, Pruessmann KP, Hennel F. MRI with zero echo time: hard versus sweep pulse excitation. *Magn Reson Med*. 2011;66:379-389.

16. Froidevaux R, Weiger M, Brunner DO, Dietrich BE, Wilm BJ, Pruessmann KP. Filling the dead-time gap in zero echo time MRI: principles compared. *Magn Reson Med*. 2018;79:2036-2045.

17. Larson PE, Han M, Krug R, et al. Ultrashort echo time and zero echo time MRI at 7T. *MAGMA*. 2016;29:359-370.

18. Greenfield S, Brostoff S, Eylar EH, Morell P. Protein composition of myelin of the peripheral nervous system. *J Neurochem*. 1973;20:1207-1216.

19. Wilhelm MJ, Ong HH, Wehrli SL, et al. Direct magnetic resonance detection of myelin and prospects for quantitative imaging of myelin density. *Proc Natl Acad Sci U S A*. 2012;109:9605-9610.

20. MacKay A, Whittall K, Adler J, Li D, Paty D, Graeb D. In vivo visualization of myelin water in brain by magnetic resonance. *Magn Reson Med*. 1994;31:673-677.

21. Laule C, Vavasour IM, Kolind SH, et al. Magnetic resonance imaging of myelin. *Neurotherapeutics*. 2007;4:460-484.

22. Varma G, Duhamel G, de Bazelaire C, Alsop DC. Magnetization transfer from inhomogeneously broadened lines: a potential marker for myelin. *Magn Reson Med*. 2015;73:614-622.

23. Glasser MF, Van Essen DC. Mapping human cortical areas in vivo based on myelin content as revealed by T1- and T2-weighted MRI. *J Neurosci*. 2011;31:11597-11616.

24. Ma YJ, Jang H, Wei Z, et al. Myelin imaging in human brain using a short repetition time adiabatic inversion recovery prepared ultrashort echo time (STAIR-UTE) MRI sequence in multiple sclerosis. *Radiology*. 2020;297:392-404.

25. Weiger M, Froidevaux R, Baadsvik EL, Brunner DO, Rosler MB, Pruessmann KP. Advances in MRI of the myelin bilayer. *NeuroImage*. 2020;217:116888.

26. Rooney WD, Johnson G, Li X, et al. Magnetic field and tissue dependencies of human brain longitudinal 1H2O relaxation in vivo. *Magn Reson Med*. 2007;57:308-318.

27. Stikov N, Boudreau M, Levesque IR, Tardif CL, Barral JK, Pike GB. On the accuracy of T1 mapping: searching for common ground. *Magn Reson Med*. 2015;73:514-522.

28. Boucneau T, Cao P, Tang S, et al. In vivo characterization of brain ultrashort-T2 components. *Magn Reson Med*. 2018;80:726-735.

29. Schirda CV, Zhao T, Andronesi OC, et al. In vivo brain rosette spectroscopic imaging (RSI) with LASER excitation, constant gradient strength readout, and automated LCModel quantification for all voxels. *Magn Reson Med*. 2016;76:380-390.

30. Noll DC. Multishot rosette trajectories for spectrally selective MR imaging. *IEEE Trans Med Imaging*. 1997;16:372-377.

31. Zahneisen B, Grotz T, Lee KJ, et al. Three-dimensional MR-encephalography: fast volumetric brain imaging using rosette trajectories. *Magn Reson Med*. 2011;65:1260-1268.

32. Olafsson VT, Noll DC, Fessler JA. Fast spatial resolution analysis of quadratic penalized least-squares image reconstruction with separate real and imaginary roughness penalty: application to fMRI. *IEEE Trans Med Imaging*. 2018;37:604-614.

33. Fessler JA, Sutton BP. Nonuniform fast Fourier transforms using min-max interpolation. *IEEE Trans Signal Process*. 2003;51:560-574.

34. Knoll F, Bredies K, Pock T, Stollberger R. Second order total generalized variation (TGV) for MRI. *Magn Reson Med*. 2011;65:480-491.

35. Uecker M, Lai P, Murphy MJ, et al. ESPIRiT---an eigenvalue approach to autocalibrating parallel MRI: where SENSE meets GRAPPA. *Magn Reson Med*. 2014;71:990-1001.

36. Jenkinson M, Smith S. A global optimisation method for robust affine registration of brain images. *Med Image Anal*. 2001;5:143-156.

37. Jenkinson M, Bannister P, Brady M, Smith S. Improved optimization for the robust and accurate linear registration and motion correction of brain images. *NeuroImage*. 2002;17:825-841.

38. Smith SM. Fast robust automated brain extraction. *Hum Brain Mapp*. 2002;17:143-155.

39. Weiskopf N, Lutti A, Helms G, Novak M, Ashburner J, Hutton C. Unified segmentation based correction of R1 brain maps for RF transmit field inhomogeneities (UNICORT). *NeuroImage*. 2011;54:2116-2124.

40. Nguyen HM, Peng X, Do MN, Liang ZP. Denoising MR spectroscopic imaging data with low-rank approximations. *IEEE Trans Biomed Eng*. 2013;60:78-89.

41. van Gelderen P, de Zwart JA, Lee J, Sati P, Reich DS, Duyn JH. Nonexponential T2 decay in white matter. *Magn Reson Med*. 2012;67:110-117.

42. Chan RW, Ramsay EA, Cunningham CH, Plewes DB. Temporal stability of adaptive 3D radial MRI using multidimensional golden means. *Magn Reson Med*. 2009;61:354-363.

43. Sati P, van Gelderen P, Silva AC, et al. Micro-compartment specific T2* relaxation in the brain. *NeuroImage*. 2013;77:268-278.

44. Wang L, Zhong X, Qian W, et al. Ultrashort echo time (UTE) imaging of receptor targeted magnetic iron oxide nanoparticles in mouse tumor models. *J Magn Reson Imaging*. 2014;40:1071-1081.

45. Jang H, Carl M, Ma Y, et al. Inversion recovery zero echo time (IR-ZTE) imaging for direct myelin detection in human brain: a feasibility study. *Quant Imaging Med Surg*. 2020;10:895-906.

46. Dvorak AV, Swift-LaPointe T, Vavasour IM, et al. An atlas for human brain myelin content throughout the adult life span. *Sci Rep*. 2021;11:269.

47. Nam Y, Lee J, Hwang D, Kim DH. Improved estimation of myelin water fraction using complex model fitting. *NeuroImage*. 2015;116:214-221.

48. Zhang J, Kolind SH, Laule C, MacKay AL. Comparison of myelin water fraction from multiecho T2 decay curve and steady-state methods. *Magn Reson Med*. 2015;73: 223-232.

49. Rahmer J, Bornert P, Groen J, Bos C. Three-dimensional radial ultrashort echo-time imaging with T2 adapted sampling. *Magn Reson Med*. 2006;55:1075-1082.

50. Gurney PT, Hargreaves BA, Nishimura DG. Design and analysis of a practical 3D cones trajectory. *Magn Reson Med*. 2006;55:575-582.

51. Yablonskiy DA, Sukstanskii AL. Biophysical mechanisms of myelin-induced water frequency shifts. *Magn Reson Med*. 2014;71:1956-1958.

52. Barmet C, De Zanche N, Pruessmann KP. Spatiotemporal magnetic field monitoring for MR. *Magn Reson Med*. 2008;60:187-197.

53. Vannesjo SJ, Graedel NN, Kasper L, et al. Image reconstruction using a gradient impulse response model for trajectory prediction. *Magn Reson Med*. 2016;76:45-58.

54. Birkl C, Birkl-Toeglhofer AM, Endmayr V, et al. The influence of brain iron on myelin water imaging. *NeuroImage*. 2019;199:545-552.

55. Sheth VR, Fan S, He Q, et al. Inversion recovery ultrashort echo time magnetic resonance imaging: a method for simultaneous direct detection of myelin and high signal demonstration of iron deposition in the brain - a feasibility study. *Magn Reson Imaging*. 2017;38:87-94.

56. Snyder AM, Connor JR. Iron, the substantia nigra and related neurological disorders. *Biochim Biophys Acta*. 2009;1790:606-614.

57. Daugherty AM, Raz N. Accumulation of iron in the putamen predicts its shrinkage in healthy older adults: a multi-occasion longitudinal study. *NeuroImage*. 2016;128:11-20.

58. Aquino D, Bizzi A, Grisoli M, et al. Age-related iron deposition in the basal ganglia: quantitative analysis in healthy subjects. *Radiology*. 2009;252:165-172.

59. Yu FF, Huang SY, Kumar A, et al. Rapid simultaneous acquisition of macromolecular tissue volume, susceptibility, and relaxometry maps. *Magn Reson Med*. 2022;87(2):781-790.

60. Sharma SD, Fischer R, Schoennagel BP, et al. MRI-based quantitative susceptibility mapping (QSM) and R2* mapping of liver iron overload: comparison with SQUID-based biomagnetic liver susceptometry. *Magn Reson Med*. 2017;78: 264-270.

61. Bozymski B, Shen X, Ozen AC, et al. Ultra-short echo time 31P 3D MRSI at 3T with novel rosette k-space trajectory. In Proceedings of the Joint Annual Meeting ISMRM-ESMRMB & ISMRT 31st Annual Meeting, London, England, UK, 2022. 1738.

62. Villarreal C, Shen X, Ozen AC, et al. Compressed sensing and the use of 3D UTE acquisition for High-resolution accelerated 23Na imaging at 3T. In Proceedings of the Joint Annual Meeting ISMRM-ESMRMB & ISMRT 31st Annual Meeting, London, England, UK, 2022. 1495.

SUPPORTING INFORMATION

Additional supporting information may be found in the online version of the article at the publisher's website.

FIGURE S1 Details of the oversampling strategy. (A) The trajectory of one petal located at *x-y* plane without using oversampling strategy. (B) The trajectory of the same petal shown in (A), but with oversampling strategy. Zoomed-in trajectories are shown at the right corner of (A) and (B) to show the locations of initial samples up to 6 m ky value. (C) The gradients waveform for (A) trajectory. (D) The gradients waveform for (B) trajectory

FIGURE S2 In vivo performance comparison between UTE sequences with 3D dual-echo rosette trajectory and 3D radial golden angle. All the images were normalized to have signal intensity from 0 to 1. (A, C, E) Reconstructed images based on compressed sensing (CS) technique from data sampled by (A) the first echo of rosette trajectory; (C) the second echo of rosette trajectory; (E) radial trajectory. (B, D, F) Reconstructed images based on regridding (RG) technique from data sampled by (B) the first echo of rosette trajectory; (D) the second echo of rosette trajectory; (F) radial trajectory. A, anterior; I, inferior; L, left; P, posterior; R, right; S, superior

FIGURE S3 Performance comparison between UTE sequences with dual-echo 3D rosette trajectory and 3D radial golden angle trajectory based on the phantom scan. All the images were reconstructed using the compressed sensing technique described in the Methods section and were normalized to have signal intensity in the range of 0 to 1. A colorbar with a reduced threshold (0 to 0.1) was used to highlight the foam pad used for positioning. The dual-echo 3D rosette sequence with ultra-short TE (20 µs) (A) detected the rapid decaying signals originating from the foam pad. However, the foam pad was not identified by the dial-echo 3D rosette sequence with longer TE (2.12 ms) (B) or by the 3D radial sequence with ultra-short TE (30 µs) (C)

FIGURE S4 Two representative subjects' results of ultra-short T$_2$ components (uT$_2$) fraction maps and ultra-short T$_2$ value maps are illustrated. (A, B) uT$_2$ fraction maps (A) and ultra-short T$_2$ value maps (B) from one volunteer. (C, D) uT$_2$ fraction maps (C) and ultra-short T$_2$ value maps (D) from another volunteer (different volunteer). A, anterior; I, inferior; L, left; P, posterior; R, right; S, superior

FIGURE S5 The results of mean frequency shift ($\Delta f_{short} - \Delta f_{long}$) after dual-exponential regression. A, anterior; I, inferior; L, left; P, posterior; R, right; S, superior

FIGURE S6 Reconstructed brain image slices based on compressed sensing technique for the dual-echo 3D rosette with TEs of 20 µs, 100 µs, 2.12 ms, 2.4 ms, and 3.6 ms from a

volunteer are shown. All the image slices were normalized to have signal intensity in the range of 0 to 1. (A) Reconstruction results from full k-space acquisition (number of petals = 36 100, 4.2 min for one dual-echo acquisition). (B) Reconstruction results from 50% k-space acquisition (undersampling factor = 2, number of petals = 18 050, 2.1 min for one dual-echo acquisition)

FIGURE S7 Reconstructed brain image slices based on compressed sensing technique for the dual-echo 3D rosette from a volunteer are shown. All the image slices were normalized to have signal intensity in the range of 0 to 1. (A) Reconstruction results of first echo and second echo from full k-space acquisition. (B) Reconstruction results of first echo and second echo from 50% k-space acquisition